ACS APPLIED MATERIALS & INTERFACES

www.acsami.org

Research Article

Polydopamine Assisted Electroless Deposition of Strongly Adhesive NiFe Films for Flexible Spintronics

Akhil K. Ramesh,[⊥] Xingyu Chen,[⊥] Ian P. Seetoh, Guo Yao Lim, Wei Xin Tan, Vasanthan Thirunavukkarasu, Tianli Jin, Wen Siang Lew, and Changquan Lai*

Cite This: *ACS Appl. Mater. Interfaces* 2025, 17, 12805−12817

Read Online

ACCESS | Metrics & More | Article Recommendations | Supporting Information

ABSTRACT: Cost-effective techniques for depositing durable magnetic thin films are essential for realizing flexible spintronic devices in wearable and soft robotics applications. Here, we introduce a highly scalable electroless deposition technique for coating ferromagnetic $Ni_{80}Fe_{20}$ thin films onto flexible polyimide and polyethylene terephthalate substrates via a polydopamine intermediate layer. The resultant films demonstrated very good adhesion strength, especially for those on polyimide substrates, which attained the highest ASTM 3359 rating of 5B and exhibited a tensile pull-off strength greater than 5.82 MPa (ASTM D4541). With the assistance of XPS and TEM results, this unusual adhesive strength of NiFe on the polymers can be traced to the formation of primary bonds across the entire coating: (i) covalent bonding between the polymer substrate and polydopamine, (ii) coordinate covalent bonding between catechol groups in polydopamine and palladium ions, and (iii) metallic bonding between palladium and NiFe. By annealing the NiFe-on-polyimide samples at 300 °C−400 °C, the crystallinity of the material was found to improve, which increased the saturation magnetization of NiFe to 1350 emu/cm^3 and decreased the coercivity to 20 Oe. Ferromagnetic resonance also showed ∼31% improvement in the film's Gilbert damping constant after annealing at 300 °C. Application of a bending strain increased the squareness ratio by 22% but decreased the saturation magnetization of the annealed film by 18%. These results suggest that the highly adhesive NiFe films on flexible polyimide substrates were of sufficient quality for spintronic devices, although their properties could be improved if the surface roughness could be decreased to that of physically deposited films.

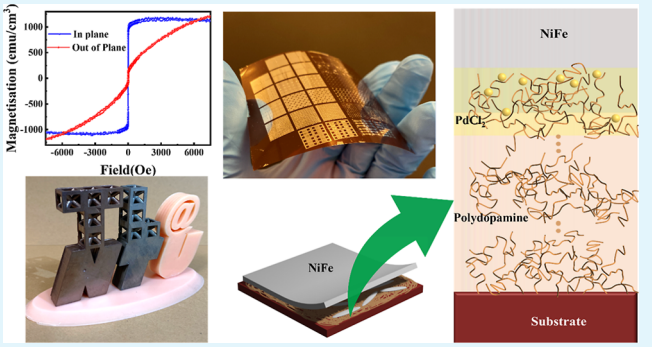

KEYWORDS: *polydopamine, electroless deposition, spintronics, adhesion, ferromagnetic thin film*

1. INTRODUCTION

Compared to conventional solid-state electronics, which depend solely on the charge of an electron to function, spintronic devices utilize the spin of an electron as an additional degree of freedom to store and process information more quickly and efficiently.[1,2] For instance, the resistance of each cell in magnetoresistive random-access memory (MRAM)[3−6] is determined by the switching of the relative magnetic orientations of two ferromagnetic thin films separated by atomically thin insulator, through an effect known as tunnel magnetoresistance (TMR).[7] Since magnetic orientations are stable in the absence of a power source, unlike electric charges used in traditional flash memory technology, MRAM is nonvolatile and thus more energy-efficient.[8]

While the majority of spintronics research and commercialization is focused on rigid planar devices, the growing interest in wearables[9,10] has also led to the integration of spintronic devices on bendable and stretchable surfaces for applications in continuous health monitoring,[11] internet of things,[12] implantable bioelectronics,[13] soft robotics,[14] and electronic skins.[15] More specifically, flexible spintronic memories[16−18] and spinvalves[19,20] had previously been demonstrated. Moreover, by combining spintronic elements with flexible electronics,[21,22] the capabilities of these devices can be significantly expanded. For instance, piezo-spintronics can aid in the harvesting of energy from mechanical sources, which is then channeled into sensing applications with self-powered operating elements.[23,24] Such devices can be used for wearable biosensors by utilizing magnetostriction for energy efficiency[25−27] and the anomalous Hall effect for sensing.[28−30]

Despite the promise of flexible spintronics, challenges persist, particularly in the deposition of functional materials on flexible substrates. For one, it is generally difficult to

Received: November 4, 2024
Revised: December 31, 2024
Accepted: February 4, 2025
Published: February 13, 2025

generate good adhesion between metallic thin films and flexible polymeric substrates due to the inherent differences in their atomic bonding, which is usually the main cause of interfacial failures, particularly under prolonged mechanical stresses induced by bending, stretching, or operational wear and tear.[17,31] In addition, the current techniques of fabricating flexible spintronics, including electron beam evaporation,[31] sputtering,[32] pulsed laser deposition,[33] molecular beam epitaxy,[34] etc., impose strict limitations in the size of the substrates due to the use of vacuum or inert-gas chambers, even though these techniques provide good adhesion.[35] The need for ultrahigh vacuum, complicated setups, and substantial energy consumption also makes these techniques relatively costly to apply. Taken together, these factors imply a relatively low manufacturing scalability for the vacuum deposition routes.

In an effort to produce cost-effective and durable flexible spintronic devices, this study focused on the development of a vacuum-free, electroless deposition (ELD) technique for coating flexible polyimide (PI) and polyethylene terephthalate (PET) substrates with a strongly adherent ferromagnetic NiFe thin film via a polydopamine (PDA) intermediate layer. PDA was necessary to improve the adhesion of the NiFe thin film on the polymer substrates, which would, otherwise, be quite poor due to the lack of strong chemical bonding between their highly dissimilar chemistries.[36,37] The adhesive strength of the NiFe film was investigated using the crosshatch tape peeling test[38−42] and tensile pull-off test,[38,43,44] with corresponding X-ray photoelectron spectroscopy (XPS) results to clarify the source behind the adhesive strengths observed. NiFe in its permalloy composition exhibits high magnetic permeability, low coercivity, and soft magnetic properties, making it well-suited for magnetic sensing and spintronic devices. To assess the viability of the NiFe films for these applications, we characterized their magnetic properties, including saturation magnetization and coercivity, in both as-deposited and annealed films. The effect of annealing on the Gilbert damping coefficient, which is crucial in the magnetization dynamics[45,46] of spintronic devices, was also determined.

2. MATERIALS AND METHODS

2.1. ELD of the NiFe Thin Film. *2.1.1. Surface Functionalization with PDA.* An aqueous solution of 0.01 M Tris hydrochloride (Roche Diagnostics, Germany) was prepared and the pH adjusted to 8.5 with the addition of NaOH. Dopamine hydrochloride (Sigma-Aldrich, USA) was then added at a concentration of 2 mg/mL.[47] The dopamine HCl oxidized in solution and self-polymerized to form a coating that was rich in catechol and amine groups.[48] Magnetic stirring was continuously employed throughout the process to prevent precipitation of polymerized dopamine, which could compromise the uniformity (conformity) of the coating. The samples were exposed to this solution at room temperature for different durations (1, 2, 4, and 24 h) to investigate the effect of PDA treatment on adhesion of NiFe.

2.1.2. Surface Activation with Pd^{2+}. After the PDA treatment, substrates were retrieved from the PDA solution and rinsed with deionized (DI) water to remove the excess particles. The substrate treated with PDA was then immersed in $PdCl_2$ (0.2 mg/mL) + HCl (40 mL/L) solution for 10 min, at room temperature, followed by rinsing with DI water. This was a surface activation step that made use of Pd^{2+} as a catalyst to initiate the ELD of FeNi.

2.1.3. Electroless Plating of NiFe Films. ELD was then performed by immersing the substrates in a slightly acidic (pH 6.5) aqueous solution (at 75 °C) using 0.06 M $Fe(NH_4)_2(SO_4)_2$ and 0.06 M $NiSO_4$ as the iron and nickel sources, respectively. The solution also contained 0.034 M dimethylamine borane (DMAB) as the reducing agent and 0.22 M lactic acid and 0.027 M diammonium citrate as the complexing agents. The process was performed for 2 to 20 min, resulting in NiFe films that were 60 nm−700 nm thick.

2.2. Materials Characterization. The surface morphology of the deposits was characterized by using field-emission scanning electron microscopy (FESEM, JEOL JSM-7600F). The accelerating voltage used was 5 kV, and the probe current was typically ∼10 μA. The chemical composition of deposits was determined using an auxiliary energy-dispersive X-ray (EDX) analyzer (Oxford Instruments) attached to the FESEM machine. X-ray diffraction (XRD, instrument: Bruker D8 ADVANCE) was performed using Cu Kα1 radiation to identify the crystalline phases in the NiFe film. The roughness of the surfaces was measured with a surface profiler (Form Talysurf i-Series PRO). The contact angles on various surfaces were measured using a goniometer (OCA 15EC, Data Physics, Germany) with and without PDA treatment, employing 5 μL of DI water. To better understand the surface chemistry at each deposition step, XPS spectra were collected over an elliptical area of 700 × 300 μm^2 using Kratos AXIS Supra (Al Kα source, 225 W). The PDA−NiFe interface was studied with the help of transmission electron microscopy (TEM, JEOL 2100f at 200 kV, Akishima, Japan), and the samples for TEM were prepared by focused ion beam (Zeiss Crossbeam 540) sectioning.

2.3. Mechanical Characterization. The adhesive strength between the NiFe film and the polymer substrates was investigated using the crosshatch test (ASTM D3359) and tensile pull-off test (ASTM D4541). A crosshatch cutter tool was used to engrave a 10 × 10 grid on the FeNi film. Subsequently, pressure-sensitive adhesive tape was applied over the incisions and firmly pressed into place. The tape was removed by swiftly pulling it off at an angle as close to 180° as possible. Following tape removal, the underlying coating was visually examined by using a magnifier.

To overcome the limitations of the above ASTM D3359 adhesive test, which is semiquantitative in nature, a tensile pull-off test (ASTM D4541) was employed to better quantify the adhesive strength. Sample surfaces, rigid support substrate surfaces (e.g., steel plate, copper plate, ceramic tile, and concrete), and steel dolly bottom surfaces with a radius of 20 mm were cleaned with ethanol and DI water. Strong adhesives (acrylic- and epoxy-based) were applied to fix the flexible substrates between a rigid support base and the steel dolly. To isolate the test area from the rest of the sample, a cutting tool was used to make a circular incision in the film with an area that corresponded to the cross-section of the dolly. A PosiTest AT-A instrument was utilized to conduct the pull-off of the dolly and record the adhesive strength.

2.4. Magnetic Property Characterization. The magnetic response of the NiFe films, including coercivity and magnetic saturation, was characterized with a vibrating-sample magnetometer (VSM, Lakeshore 7400). In-plane ferromagnetic resonance (FMR) measurements were also conducted using a custom vector network analyzer (VNA) to sweep the DC field (H_{ext}) from 4000 to 0 Oe at a constant microwave frequency (f). The RF signal from the VNA (Keysight N5224A) was first directed to the signal line of the coplanar waveguides (CPW) to generate the RF magnetic field (h_{rf}). The sample was positioned in a flip-chip configuration, ensuring direct contact between its surface and the CPW. Upon microwave excitation, the ferromagnetic layer underwent precession around the effective magnetic field. At resonance, the RF frequency (h_{rf}) aligned with the precession frequency of the magnetization in the sample, so that absorption of RF energy occurred. This was detected by an RF diode connected to the lock-in amplifier (Zurich Instruments MFLI), which enhanced the signal-to-noise ratio.[49] The measurement process was repeated for various frequencies within the 10−16 GHz range to obtain the Gilbert damping coefficient of the ferromagnetic film, which helps in defining the functionality of the film.

3. RESULTS AND DISCUSSION

3.1. ELD of Metallic Films on Nonmetallic Substrates. *3.1.1. Surface Characteristics.* The ELD of the NiFe thin film on flexible PI and PET substrates was a 3-step process that

https://doi.org/10.1021/acsami.4c19118
ACS Appl. Mater. Interfaces 2025, 17, 12805−12817

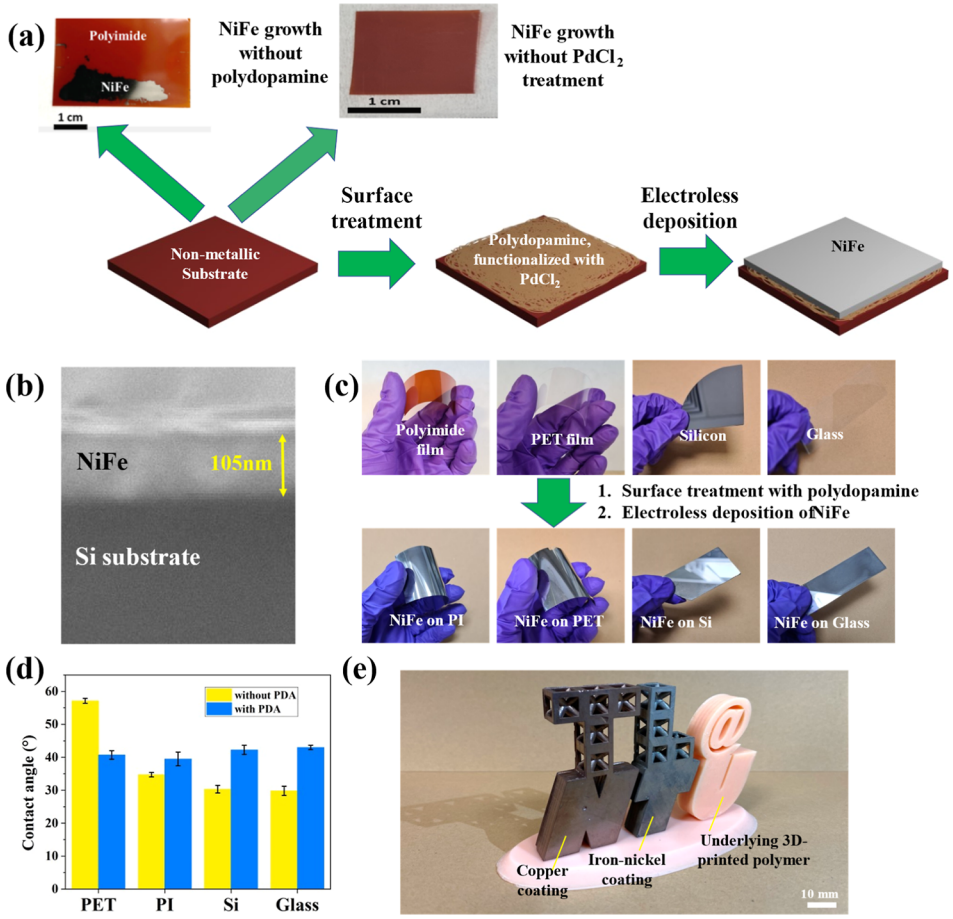

Figure 1. (a) Schematic illustration of the overall process to produce NiFe thin films on nonmetallic substrates. (b) Uniform NiFe film formed on the Si substrate after 4 min of ELD. (c) ELD of NiFe on flexible PI, flexible PET, rigid Si, and rigid glass substrates, after 24 h PDA coating. (d) Water contact angles of different substrates before and after 24 h PDA coating. (e) NiFe and Cu coatings applied to selective parts of a polymeric structure 3D-printed with DLP.

involved (i) surface functionalization with PDA, (ii) surface activation with Pd^{2+} ions, and (iii) metal film deposition (Figure 1a). The surface functionalization and surface activation were essential to the coating process, as the absence of the PDA layer resulted in very poor coverage of NiFe (Figure 1a, inset), while there would be no visible growth of the NiFe, even after an hour, if Pd^{2+} ions were not introduced to the surface. In the presence of PDA and Pd^{2+}, uniform adherent NiFe coatings were observed to form at a rate of ~25 nm/min (Figure 1b). EDX analysis revealed a Ni−Fe atomic ratio of 78:22 for the coatings, which is indicative of the permalloy composition ($Ni_{80}Fe_{20}$).

As a demonstration of the versatility of this 3-step ELD process, we show that NiFe can also be successfully deposited on rigid Si and glass substrates using this technique (Figure 1c). Water contact angles on the flexible PI, flexible PET, rigid Si, and rigid glass substrates after surface functionalization with PDA were consistently ~40°, indicating that the PDA layer was successfully coated onto the substrate surfaces, regardless of their initial degree of hydrophilicity (Figure 1d). Furthermore, the procedure was also compatible with other metallic coatings such as Cu, Ni, etc., and produced a uniform coating even on relatively large and highly complex structures that could not be easily coated well with conventional physical and chemical vapor deposition techniques (Figure 1e).

3.1.2. X-ray Photoelectron Spectroscopy. The presence of each intermediate layer in the NiFe coating was further confirmed through XPS wide scans and high-resolution scans after every deposition step (Figure 2). For pristine PI (Figure 2a), characteristic peaks for carbon (C), nitrogen (N), and oxygen (O) atoms were detected, while PET (Figure 2b) initially exhibited only signals for C and O atoms until PDA was deposited. This is expected, as PI contains nitrogen but PET does not. This was confirmed from the fitting of N 1s spectra of PI with peaks at ~400.4 eV (imide) and ~398.5 eV (aromatic N/R = N−R).

After surface treatment with PDA, the N 1s spectra show the presence of amine groups in both PI/PDA and PET/PDA samples. Peak fitting of the N 1s spectra revealed 3 peaks in the PDA-coated PI and PET substrates. In both cases, the peak at ~399.9 eV corresponds to primary amines (R-NH_2) and the peak at ~402.1 eV indicates secondary amines (R-NH-R), likely formed during the initial stages of polymerization. The peak at ~398.4 eV in PI/PDA samples indicates the presence of imines or tertiary/aromatic amines (R = N−R), which were formed in the later stages of polymerization.[50−52] However, for the PDA-coated PET, the third peak at ~402.7 eV indicates that R-NH_3^+ was formed as a part of the spontaneous proton transfer from the catechol to amine.[53]

The fitting of the PI substrate's C 1s spectra indicated C═C/C−C/CH_x at ~284.5 eV, C−OH/C−N at ~286.0 eV, C═

https://doi.org/10.1021/acsami.4c19118
ACS Appl. Mater. Interfaces 2025, 17, 12805−12817

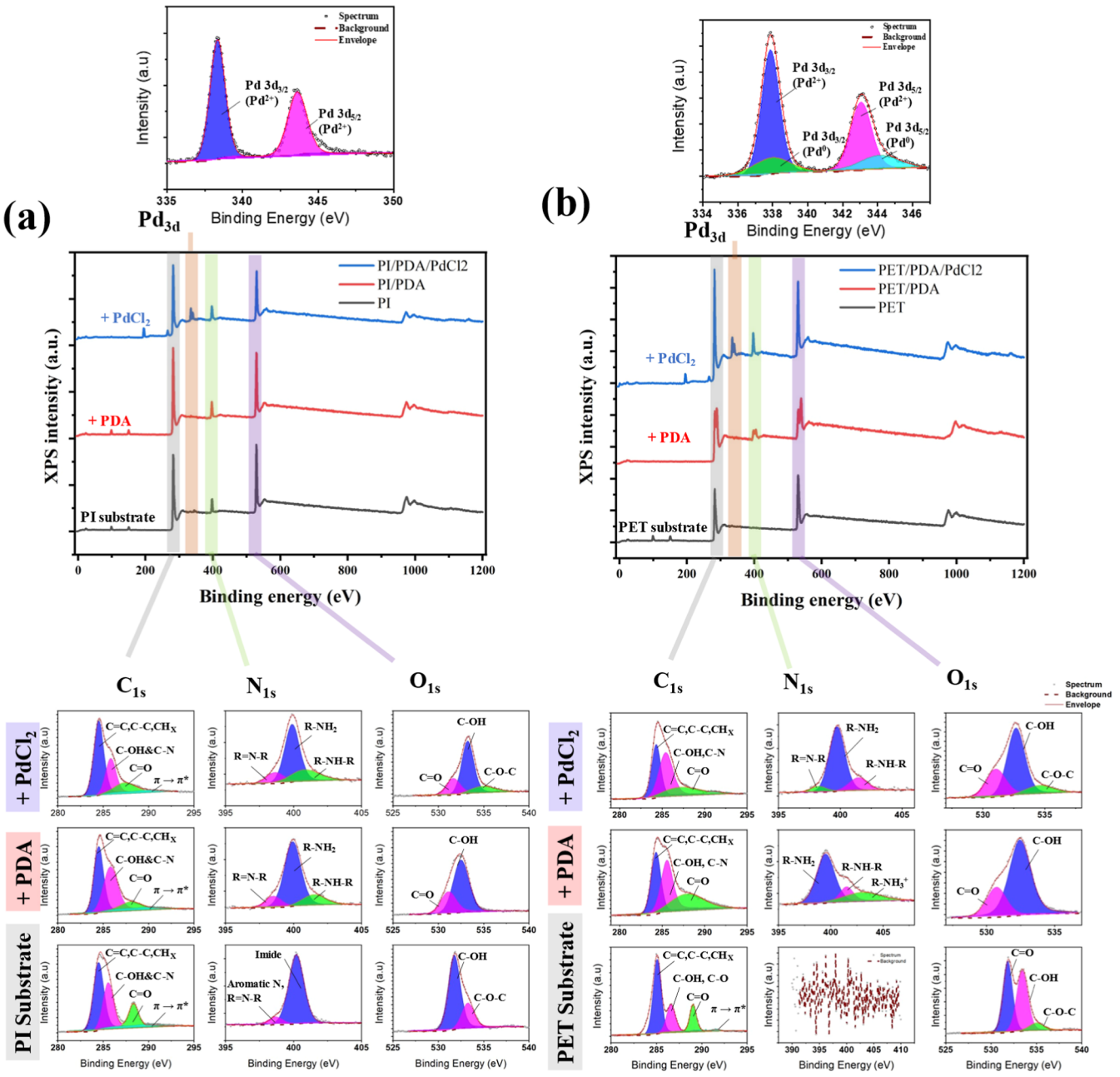

Figure 2. XPS wide-scan spectra and their corresponding fitted high-resolution spectra showing the various chemical species attached to the substrate at different stages of ELD (plain substrate, 24 h PDA treatment and surface activation using Pd^{2+}) on (a) PI and (b) PET substrates.

O at ~288.2 eV, and a $\pi \rightarrow \pi^*$ shake-up peak at ~290.3 eV. Similar to PI, the C 1s spectra of the PET substrate were also fitted with 4 components, in which C−O was observed at ~286.0 eV instead of C−N. Furthermore, after the surface treatment with PDA and surface activation using $PdCl_2$, the $\pi \rightarrow \pi^*$ shake-up peaks could not be distinguished in PET due to broadened C═O peaks. The fitting of the O 1s spectra in both substrates also confirmed the presence of C═O (~531.9 eV) coming from the carbonyl groups in the PI or PET substrate, while the major peak at ~533.2 eV was from the catechol (C−OH) groups. After $PdCl_2$ surface activation, the $3d_{5/2}$ component of Pd_{3d} spectra in the $PdCl_2$/PDA/PI stack was detected at ~338.3 eV, indicating the possibility of Pd^{2+} forming $[PdCl_2(CH_3(CN)_2)]$ and similar compounds[54] which facilitated chelation.[55]

3.1.3. Transmission Electron Microscopy. To gain a deeper understanding of the film microstructures and interface bonding structures, cross-sectional TEM analysis was performed. This analysis provided crucial insights into the interfacial bonding between the NiFe film and the PDA intermediate layer. The TEM images, along with energy-dispersive X-ray spectroscopy (EDS) mapping, revealed an intrusion of NiFe into the PDA layer; that is, adjacent to a pure PDA layer was a diffused layer where PDA and NiFe were co-deposited (Figure 3a). The lack of a clean interface between PDA and NiFe suggests that delamination cracks cannot propagate easily between the 2 materials, which may contribute to a strong interfacial adhesion between PDA and NiFe. Furthermore, the selected area electron diffraction (SAED)

https://doi.org/10.1021/acsami.4c19118
ACS Appl. Mater. Interfaces 2025, 17, 12805−12817

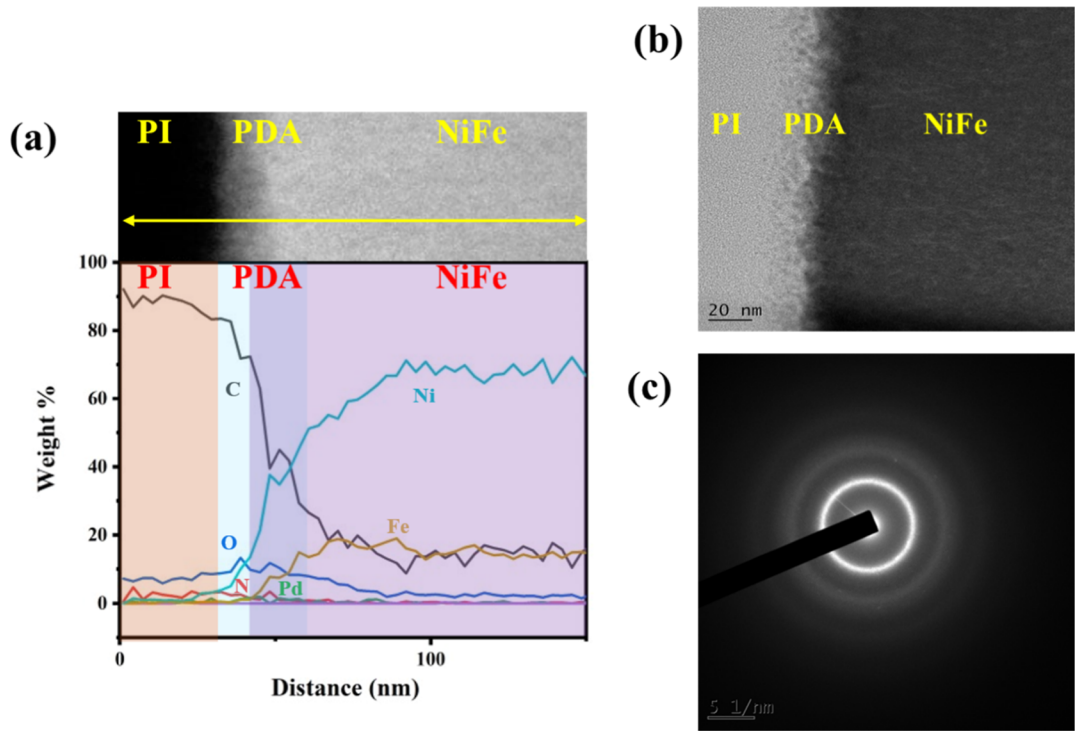

Figure 3. (a) TEM−EDS line scan at the NiFe/PDA interface on the PI substrate, showing the distribution of elements across the PI substrate, PDA layer, and NiFe thin film, with clear evidence of NiFe intrusion into the PDA layer; (b) cross-sectional TEM image of the NiFe/PDA/PI structure and (c) SAED pattern of the NiFe thin film.

results suggest that the as-deposited NiFe films were mainly amorphous with polycrystalline domains.

3.2. Adhesive Strength. *3.2.1. Mechanical Tests.* The adhesive strength between the NiFe coatings and substrates was first determined using the qualitative ASTM D3359 crosshatch peel test (Figure 4a). A 10 × 10 grid was cut into the NiFe film, and a tape was subsequently pressed onto the grid. After peeling the tape off, the grid was visually examined to determine the extent of coating removal. Comparing the experimental results with the ASTM classifications, the adhesive strength was then assigned a grade. The crosshatch test was applied to NiFe coated on flexible PI and flexible PET substrates, for 4 h and 24 h of surface functionalization with PDA.

The adhesive strength of NiFe on PET surfaces treated with PDA for 4 h achieved only a 1B ASTM classification, as a relatively large extent of the NiFe film in the 10 × 10 grid was removed (Figure 4a). XPS analysis of the detached regions (Figure 4c) showed that the PDA layer was absent (N signal missing), indicating that the film had delaminated from the PDA−PET interface and not the NiFe/PDA interface. Increasing the duration of PDA functionalization to 24 h improved the adhesive strength of NiFe on PET significantly, to the second-best classification of 4B.

In contrast, the adhesive strength of NiFe on the PI substrates was found to be relatively insensitive to the PDA functionalization duration. It was remarkably resistant against the peel-off attempts, and there was no discernible detachment from the substrate (Figure 4b). This result indicates a strong adhesion between the substrate and the coating and earned it the highest ASTM rating of 5B. To further investigate this strong adhesion between PI and NiFe, crosshatch peel tests were conducted on samples treated with 2 and 24 h of PDA functionalization for varying NiFe deposition durations (Figure 4d). It was found that at a shorter PDA functionalization duration of 2 h, 120 nm of NiFe could still attain 5B classification, but it began detaching from the substrate when the thickness was ∼270 nm and peeled off significantly when the NiFe thickness reached 450 nm. The main reason thicker coatings had a tendency to flake was likely because of the high interfacial stress between NiFe and PDA,[56] which grew larger as the films became thicker. To delay the onset of this stress-induced disintegration of the NiFe film, the PDA functionalization duration was increased to 24 h, which allowed the adhesive strength of NiFe on PI to retain the 5B classification until a thickness of 780 nm. At longer growth durations (≥20 min), NiFe was observed to spontaneously flake off from the substrates.

In addition to the qualitative ASTM D3359 crosshatch peel test, ASTM D4541 tensile pull-off tests were also conducted to quantify the adhesive strength of the NiFe coating on PI. The test involved attaching the sample to a rigid backing plate on one end and a steel dolly on the other (Figure 5a). The adhesive strength can be found by measuring the tensile stress required to pull the dolly off the surface and examining the location of interfacial failure, which could take place via (i) cohesive fracture (within a coating layer), (ii) adhesive fracture (at the interface between layers), or (iii) glue failure (visible separation of the glue from itself, the coating, or the dolly).

Based on the results of 4 attempts shown in Table 1, it can be observed that the steel dolly was always detached from the sample due to glue failure, without delamination of NiFe from the PI substrate (Figure 5b). Therefore, the readout of 1.53−5.82 MPa in Table 1 is indicative of the adhesive strength of the glue, while the bonding strength between NiFe and PI can only be surmised as greater than 5.82 MPa (Figure 5c). This

https://doi.org/10.1021/acsami.4c19118
ACS Appl. Mater. Interfaces 2025, 17, 12805−12817

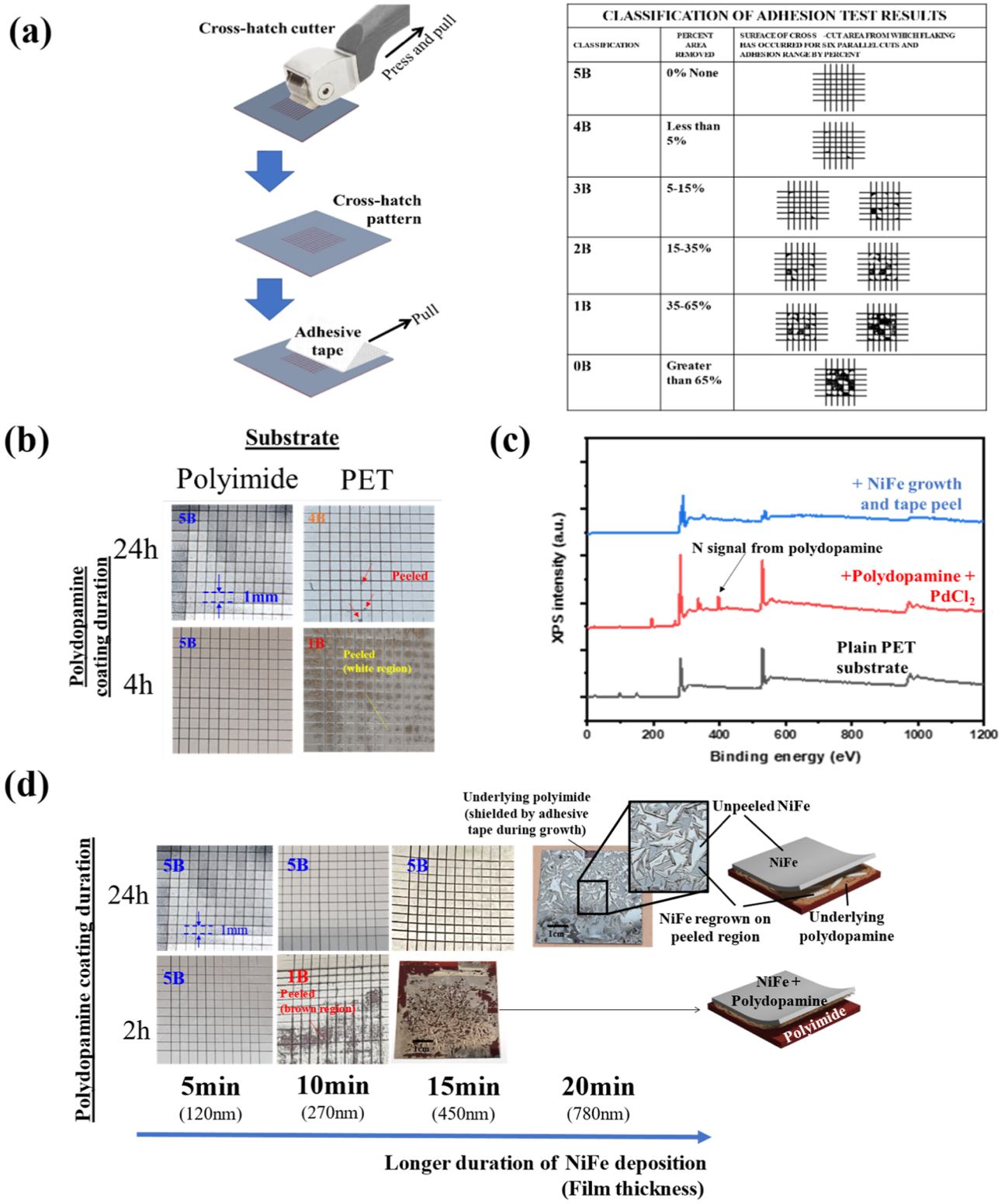

Figure 4. (a) Illustrations of the ASTM D3359 procedure and classification. (b) Crosshatch tape peel tests on ~100 nm NiFe deposited on PI and PET substrates. (c) XPS analysis of the PET-based, 4 h-PDA treatment sample after NiFe is peeled off. (d) Crosshatch tape peel tests on NiFe deposited on PI substrates, for different durations of PDA treatment and NiFe deposition.

lack of NiFe delamination for the pull-off test was consistently observed even with the use of various other adhesive glues (epoxy- and acrylic-based) and rigid backing plates (copper, ceramics, and concrete; see Supporting Information Table S1), where either the glue failed or the support substrate was damaged. Further efforts at improving glue adhesion of the sample to the rigid support resulted in other glue failure modes (Supporting Information Table S2) but none involving the delamination of the NiFe film from PI.

3.3. Magnetic Properties. To assess the suitability of utilizing the electrolessly deposited NiFe films for flexible spintronics devices, their magnetic properties were charac-

https://doi.org/10.1021/acsami.4c19118
ACS Appl. Mater. Interfaces 2025, 17, 12805−12817

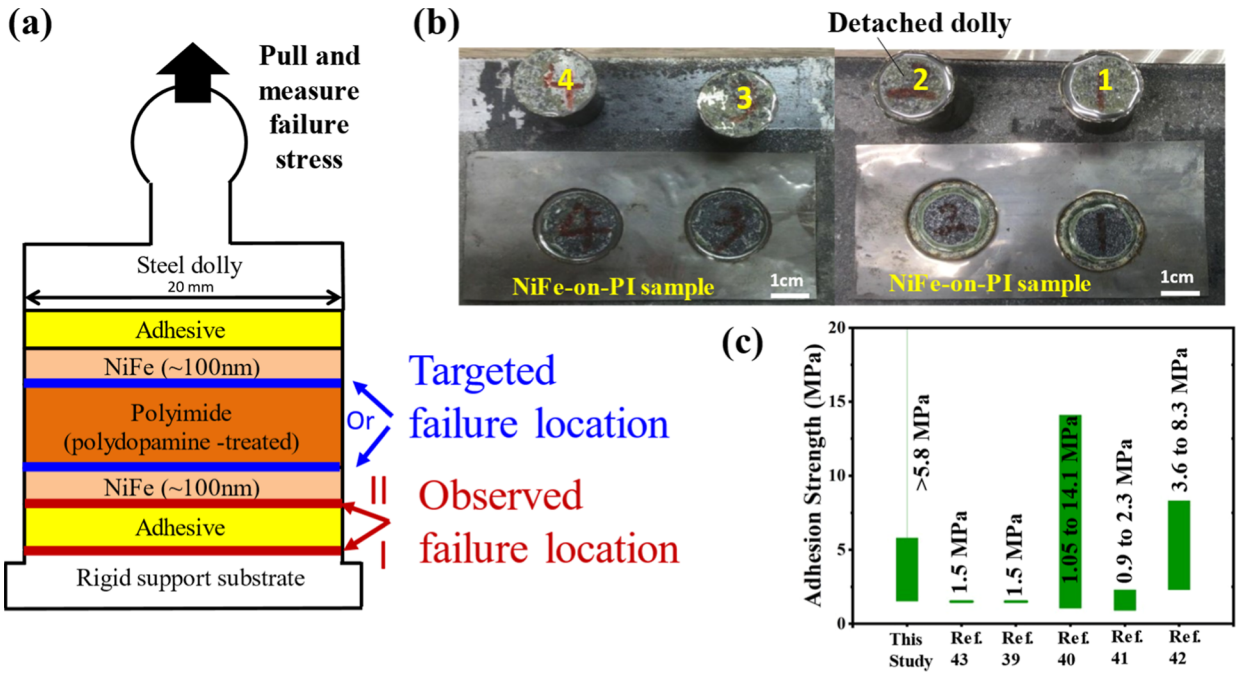

Figure 5. (a) Schematic diagram showing the sample preparation for the ASTM 4541 tensile pull-off test and the potential interfacial failure locations. (b) Photographs showing the results of the 4 tests recorded in Table 1. (c) Comparison chart for adhesion strength with the recent literature.

Table 1. Tensile Pull-Off Test (ASTM D4541) Results on NiFe-On-PI Samples

	adhesive ID	rigid support substrate	delamination locations	adhesive strength (MPa)
test #1	M (acrylic-based)	steel plate	I (30%), II (70%)	1.53
test #2	M (acrylic-based)	steel plate	I (20%), II (80%)	2.36
test #3	M (acrylic-based)	steel plate	I (10%), II (90%)	5.82
test #4	M (acrylic-based)	steel plate	I (50%), II (50%)	2.87

terized with a VSM. From Figure 6a,b, it can be observed that the magnetic saturation of the as-deposited NiFe film was low (~500 emu/cm^3), while its coercivity was relatively high (~28 Oe), compared to NiFe obtained through vacuum techniques.[57] This is likely because the as-deposited films exhibited a predominantly amorphous structure with small polycrystalline domains, as indicated by the SAED results above and supported by the XRD results in Figure 6c. In addition, defects or residual interfacial stresses[56] generated during the growth of the NiFe film in solution may also have contributed to these poor magnetic properties.

Therefore, in an attempt to improve the magnetic performance of the NiFe films, the samples were annealed for 1 h in a nitrogen atmosphere at varying temperatures up to 500 °C, which was the highest operating temperature for Kapton PI, according to dynamic mechanical analysis and TGA measurements (Supporting Information). The results in Figure 6a,b showed that the magnetic saturation improved almost linearly with annealing temperature to a maximum of ~1350 emu/cm^3 at 400 °C annealing temperature, before falling drastically to ~400 emu/cm^3 after 500 °C of annealing. The coercivity, on the other hand, reached a minimum of 20 Oe at 300 °C of annealing temperature and a maximum of 58 Oe at 500 °C.

XRD results show that this improvement can largely be attributed to the recrystallization and grain growth of the as-deposited NiFe (Figure 6c). Upon annealing at 400 °C for 1 h, the amorphous film crystallized into a polycrystalline FCC structure with a strong (111) texture and the crystal size was observed to increase from 27.8 to 80 Å (Figure 6c,d; Supporting Information). Previous studies have also shown that larger grains lead to improved magnetic saturation and lower coercivity in NiFe.[58] However, the deterioration of magnetic properties at 500 °C was probably due to substrate degradation as TGA results of PI indicate that the material undergoes 40% of weight loss at around 500 °C (Supporting Information Figure S1).

To further explore the spintronics capability of the film, the field-swept in-plane FMR spectra for a ~100 nm thick NiFe sample on PI were recorded for frequency (f) values ranging from 11 to 15 GHz (Figure 7a). The FMR spectra at each f value were fitted with a derivative of the Lorentzian function to extract the resonance field (H_r) and the line width (ΔH) of the spectra for each frequency[59]

$$Y = -S\frac{\left(\frac{\Delta H}{2}\right)^2 (H_{ext} - H_r)}{\left(\left(\frac{\Delta H}{2}\right)^2 + (H_{ext} - H_r)^2\right)^2} + A\frac{\left(\frac{\Delta H}{2}\right)\left(\left(\frac{\Delta H}{2}\right)^2 - (H_{ext} - H_r)^2\right)}{\left(\left(\frac{\Delta H}{2}\right)^2 + (H_{ext} - H_r)^2\right)^2} \quad (1)$$

Here, S and A represent the symmetric and antisymmetric absorption coefficients, respectively. The frequency dependence of H_r and ΔH for all samples was subjected to fitting

https://doi.org/10.1021/acsami.4c19118
ACS Appl. Mater. Interfaces 2025, 17, 12805−12817

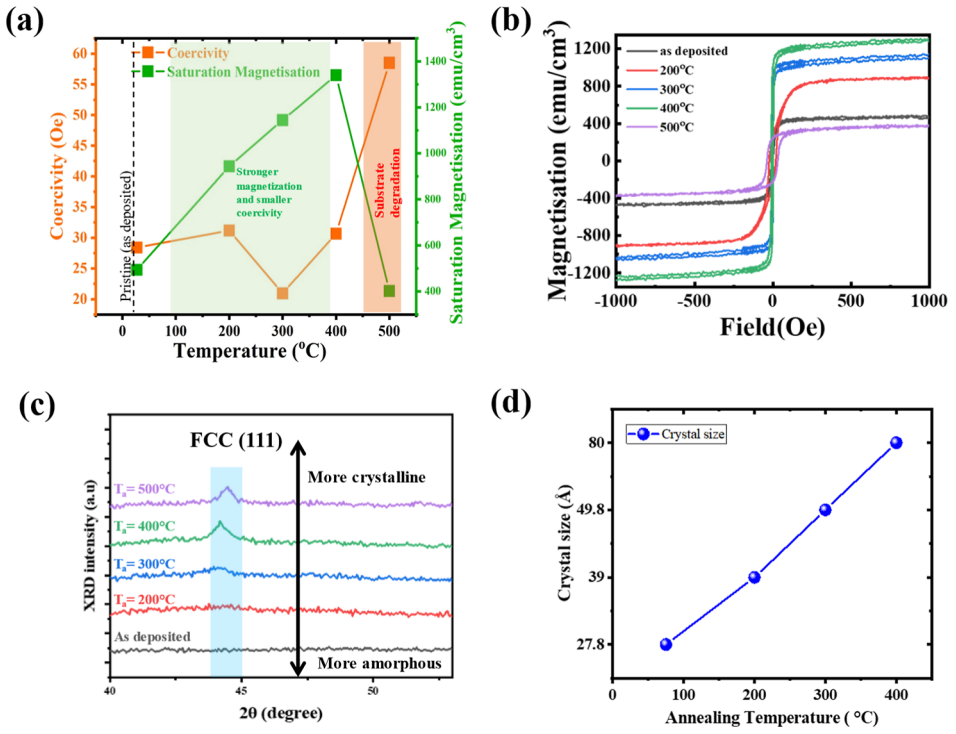

Figure 6. (a) Saturation magnetization and coercivity of NiFe-on-PI films after thermal annealing at different temperatures, along with (b) corresponding magnetic hysteresis curves and (c) XRD spectra showing the improvement in crystallinity of the sample toward FCC(111) as the sample is annealed to higher temperature. (d) Effect of annealing temperature on crystallite size of electroless-deposited NiFe based on the glancing-incidence X-ray diffraction (GIXRD) results.

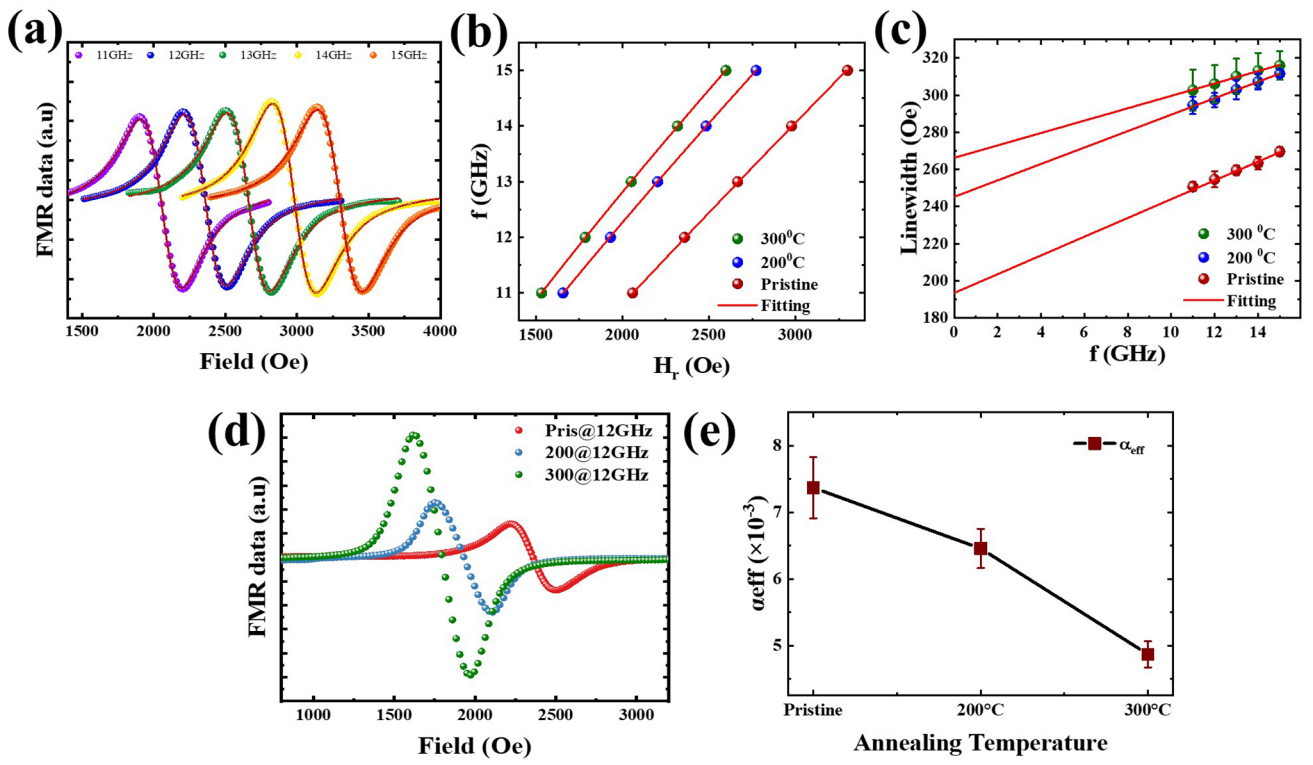

Figure 7. (a) Frequency-dependent FMR spectra recorded for the pristine ELD NiFe film. Frequency dependence of the (b) resonance field (H_r) and (c) line width (ΔH) for the as-deposited and annealed samples. Data points indicate experimental results and red line shows fitting. (d) Comparison of FMR spectra of the as-deposited and annealed samples (200 and 300 °C) for 12 GHz. (e) Trend of damping constant of electroless deposited NiFe film with annealing temperature.

https://doi.org/10.1021/acsami.4c19118
ACS Appl. Mater. Interfaces 2025, 17, 12805−12817

using Kittel's equation and the line width equation (eqs 2 and 3), as illustrated in Figure 7b,c

$$f = \frac{\gamma}{2\pi}\sqrt{(H_r + H_k)(H_r + H_k + M_{eff})} \quad (2)$$

$$\Delta H = \Delta H_0 + \frac{4\pi\alpha_{eff} f}{\gamma} \quad (3)$$

where γ represents the gyromagnetic ratio, H_k denotes the magnetic anisotropy field, M_{eff} signifies the effective saturation magnetization, and ΔH_0 refers to the frequency-independent line width contribution due to film inhomogeneity. The expression $\gamma = g\mu B/\hbar$ defines the gyromagnetic ratio, in which $\hbar$ is the reduced Planck's constant, g stands for the Lande "g" factor (2.14 for electrons in permalloy),[60] and μB represents the Bohr magneton. The effective damping constant (α_{eff}) for the NiFe film was calculated by fitting eq 3.

Figure 7d shows the effect of the annealing temperature on the effective damping constant, α_{eff}. It decreases with an increase in temperature up to 300 °C (from 0.0071 ± 0.0004 to 0.00487 ± 0.0002) due to the enhancement in crystallinity at higher temperatures.[61] The value of α_{eff} found in these 100 nm NiFe films is higher than previous reports, which could be due to the increased surface roughness of the film.[46,62] The film roughness in our samples varied between 28 nm and 68 nm depending on the PDA treatment duration (Supporting Information), while it is normally less than 10 nm for physical vapor-deposited films.[62] To enhance magnetic properties, surface roughness can be reduced by this approach, enabling thinner films more suitable for spintronic applications as the current ∼100 nm thickness is better suited for magnetic sensing.

To demonstrate the potential of the NiFe films for flexible magnetic sensing applications, we conducted VSM measurements under both strained (bending) and nonstrained conditions. To induce mechanical strain, the films were bent over 3D-printed molds with a radius of curvature of 6 mm. The results indicate that the squareness ratio (i.e., the ratio of remanence magnetization to saturation magnetization) increased from 46% to 56% upon bending (Figure 8). Additionally, the saturation magnetization decreased from 0.0066 to 0.0054 emu. These changes arise from the intrinsic magnetostriction effect in permalloy films, which aligns the magnetic anisotropy along both the stress direction and the magnetic easy axis[63] and is key to the operating principle of a flexible spintronic sensor.

4. DISCUSSION

4.1. Comparison of Adhesive Strength with the Literature. The excellent adhesive strength of NiFe films on PI is all the more remarkable when compared with results reported for other ELD techniques. In both ASTM D3359 and ASTM D4541 testing, the NiFe-PI bonding strength measured here is consistently one of the highest, if not the highest, in the literature. Importantly, this adhesive strength does not require roughening or etching of the substrate surface, which would, in turn, lead to significant surface roughness in the deposited metallic film, negatively affecting its viability for spintronics device fabrication.[57] Furthermore, compared to the other ELD methods (Table 2), our PDA-based method is (i) simpler (fewer processing steps and chemicals), (ii) more scalable (no vacuum processes like plasma etching), and (iii) more versatile; most methods from the literature are highly specific

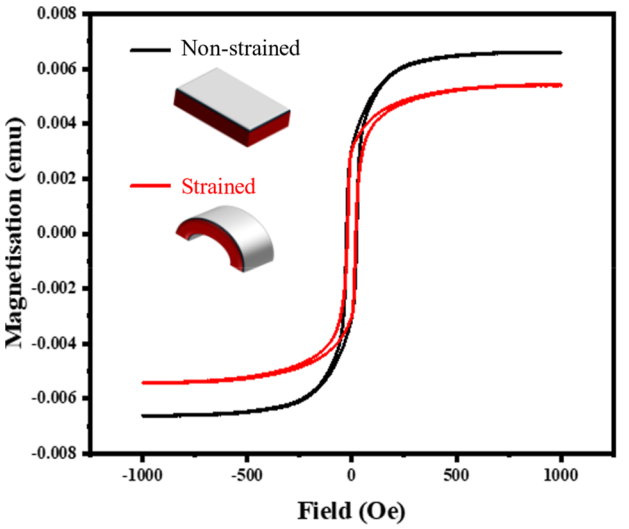

Figure 8. Magnetization curves for ∼100 nm NiFe thin films on a PI substrate under strained (bent) and nonstrained (flat) conditions, along with a schematic illustration of the PI/NiFe system in both states.

to one type of substrate, while the compatibility of the present technique with substrates of different chemistry and rigidity had already been demonstrated in Figure 1e.

4.2. Mechanisms for Strong Bonding between NiFe, PDA, and PI. Based on the XPS and TEM−EDS results, and previous information on PDA bonding in the literature, some possible mechanisms for the outstanding NiFe adhesion to polymer substrates are proposed in Figure 9. We start off by noting that there are similarities between the PI and PET polymers—for each repeating unit in the polymer, PI contains 4 carbonyl groups, 2 oxydianiline benzene rings (ODA), and 1 pyromellitic dianhydride (PMDA) benzene ring,[67] while PET contains 2 carbonyl groups and 1 ODA benzene ring. While the exact structure of the PDA coating remains uncertain,[36] it is widely accepted that PDA contains catechol groups with amine and hydroxyl pendant groups. Based on these structures, there is a range of bonding possibilities between PDA and polymeric substrates.

First, the amine groups in PDA may combine with the carbonyl groups in PI and PET to form imine cross-links. Second, the benzene rings in both the PDA and polymers can also form covalent bonds through radical coupling.[68] Third, Schiff-base reaction may occur between the amine groups in PDA and the carbonyl groups in the polymers.[69] Other than primary bonding, secondary bonds other than van der Waals' forces can also be expected. For instance, hydrogen bonding can occur between the carbonyl groups of the polymers and hydroxyl groups in PDA,[70] as well as $\pi-\pi$ stacking between the PDA catechol groups and benzene rings in the polymeric substrates.[68]

The above bonding mechanisms between PDA and the polymeric substrates are expected to increasingly develop as the polymerization of the dopamine, which involves the formation of intermediates (e.g., 5,6-dihydroxyindole[47,48,51]) and complexes, proceeds over time by oligomerization. This explains why the adhesive strength of NiFe on PET (Figure 4b) and 450 nm of NiFe on PI (Figure 4d) improved significantly when the duration of PDA deposition was increased. In addition, based on the above analysis, the extraordinary adhesive strength of NiFe on PI compared to

https://doi.org/10.1021/acsami.4c19118
ACS Appl. Mater. Interfaces 2025, 17, 12805−12817

Table 2. Tensile Pull-Off (ASTM D4541) Results for NiFe-On-PI Samples, Compared with Those of Other Coating−Substrate Combinations from the Literature

			surface treatment before ELD				
	substrate	film	key steps	surface etch	metal film R_a roughness (nm)	ASTM D4541 pull-off adhesion strength (MPa)	ASTM D3359 crosshatch tape test classification
present study	PI	NiFe	PDA coating	no	68.4	>5.8	5B
Wang et al. (2017)[64]	PI	Cu	hydrolyze in NaOH. apply heat curable Pd complex ink	no	N.A.	N.A.	5B
Park et al. (2017)[44]	PET	Cu	oxygen plasma	yes	N.A.	N.A.	5B
Zhang et al. (2018)[38]	PDMS	Cu	PDA-assisted with Ag^+ catalyst and Plasma	yes	311	N.A	5B
Vasconcelos et al. (2021)[43]	nitrile butadiene rubber	Ni	PDA coating, oxidized using $CuSO_4/H_2O_2$	no	N.A.	1.5	4B
Chan et al. (2022)[39]	3D-printed shape memory polymers	Cu	UV/ozone plasma. polyethylenimine coating	yes	9.7−33.4	1.5	N.A
Georgieva et al. (2022)[40]	ABS	Ni	swell with acetone. etch in sulfuric acid	yes	113.8	1.05−14.1	N.A
Nian et al. (2016)[41]	PC/ABS alloy	Ni	swell with phosphoric acid. etch in H_2O_2/H_2SO_4	yes	N.A.	0.9−2.3	N.A
Tsai et al. (2022)[42]	polyamide	Cu	cold-spray of Cu particles	yes	6120−6580	3.6−8.3	N.A
Akin et al. (2023)[65]	3D-printed polymers	Cu	cold-spray of Cu particles	yes	3240−3470	2.84	5B
Rauta et al. (2024)[66]	Mg alloy sheet	Ni−W−P	aqueous iron sulfate solution	yes	N.A	6.2−8.1	4B

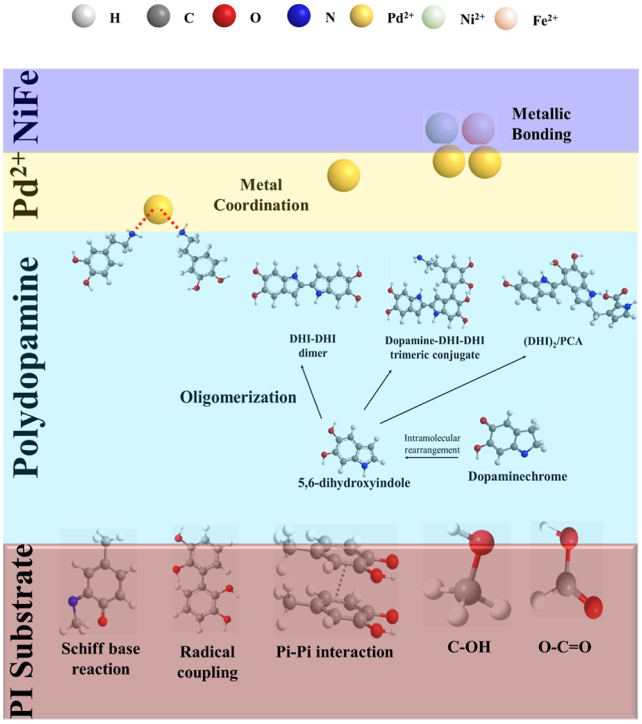

Figure 9. Schematic model for possible bonding between the layers in NiFe on PI.

that on PET may be due to the relative abundance of carbonyl groups (4 per repeating unit for PI vs 2 for PET), benzene rings (3 per repeating unit for PI vs 1 for PET), and succinimide rings (2 per repeating unit for PI vs 0 for PET), all of which can be expected to participate in the primary and secondary bonding mentioned above.

Next, the chelation of Pd^{2+} ions by PDA during the surface activation step is expected to take place through metal coordination interactions with PDA's hydroxyl groups.[70] The presence of the Pd on the PDA surface then acts as a catalyst for the reduction of NiFe by DMAB,[47] which is expected to form metallic bonds with Pd. The cross-section TEM image and the TEM−EDS data support this postulation as there was clearly a diffuse layer where PDA and NiFe were co-deposited (Figure 3a). In addition, TEM−EDS analysis also verified the presence of Pd at this boundary, strongly implying that chelation between Pd and PDA and the formation of metallic bonds between Pd and NiFe were present. Additionally, the higher weight percentages of oxygen and carbon detected at the other interface further support the proposed mechanism outlined below.

In summary, the above analysis suggests that the strong NiFe adhesion on the polymer substrates can be attributed to the primary bonds formed at every interface throughout the polymer-PDA-Pd-NiFe stack. Comparing the two flexible substrates, however, the presence of more functional groups in PI may have helped produce stronger bonding between PDA and PI, compared to PET.

While the thickness of the NiFe films in this study exceeds the optimal range typically employed in spintronics applications, we recognize this as a current limitation. Nevertheless, this work provides foundational insights into achieving robust adhesion of NiFe films on flexible polymer substrates through a cost-effective, nonvacuum ELD method. These findings on film−substrate bonding are essential for the future development of thinner electroless-deposited NiFe films suitable for spintronic device applications.

5. CONCLUSIONS

Thin films of NiFe alloy (~100 nm) were successfully deposited onto rigid and flexible surfaces of different

https://doi.org/10.1021/acsami.4c19118
ACS Appl. Mater. Interfaces 2025, 17, 12805−12817

hydrophilicity, including complex 3D-printed geometries, using a highly versatile process involving PDA-assisted ELD. Activation of the PDA-coated substrates with palladium ions during ELD yielded highly adhesive NiFe films on flexible PI and PET substrates.

Adhesion strength tests were performed for a qualitative and quantitative understanding of NiFe adhesion on PI and PET substrates. Crosshatch ASTM D3359 tape testing indicated that NiFe on PI samples achieved the highest ASTM rating of 5B, even when the duration of PDA coating was short. 24 h PDA treatment was required for NiFe on PET to attain a ASTM rating of 4B. The NiFe-on-PI samples were also highly resistant to tensile pull-off by superadhesives during ASTM D4541 testing, with test readouts suggesting the adhesion strength to be much greater than 5.8 MPa. This value compares well with other electroless-deposited metal films in the literature, with our surface treatment process being economical, simpler, and more versatile. The possible adhesion mechanisms include covalent and noncovalent interactions at the PDA−substrate interface, catechol-ion coordination at the PDA−Pd^{2+} interface, and metallic bond formation at the Pd^{2+}−NiFe interface. These mechanisms were supported by XPS results, which indicated that the interactions between PDA, Pd^{2+}, and the underlying substrate played a crucial role in the adhesive strength of the NiFe coating.

Furthermore, the saturation magnetization and coercivity of the NiFe films on the PI substrate were found to increase and decrease, respectively, with annealing, largely because of improved crystallinity. A magnetization dynamics assessment further revealed the film's suitability for fast-switching spintronic applications as the Gilbert damping coefficient of the pristine sample decreased from 0.0071 to 0.0048 after annealing at 300 °C. VSM measurements of the NiFe film indicated that the squareness ratio increased from 46% to 56%, while the saturation magnetization decreased from 0.0066 emu to 0.0054 emu when the films were subjected to bending strain. These results collectively indicate that the PDA-mediated NiFe films are viable for use as flexible spintronic sensors.

■ ASSOCIATED CONTENT

Data Availability Statement

The data that support the findings of this study are available within the article and its Supporting Information.

Supporting Information

The Supporting Information is available free of charge at https://pubs.acs.org/doi/10.1021/acsami.4c19118.

Thermal stability of the flexible substrate, adhesion testing, film morphology, and GIXRD results (PDF)

■ AUTHOR INFORMATION

Corresponding Author

Changquan Lai − *Temasek Laboratories, Nanyang Technological University, Singapore 637553, Singapore; School of Materials Science & Engineering and School of Mechanical & Aerospace Engineering, Nanyang Technological University, Singapore 639798, Singapore;* orcid.org/0000-0003-0202-4738; Email: cqlai@ntu.edu.sg

Authors

Akhil K. Ramesh − *Temasek Laboratories, Nanyang Technological University, Singapore 637553, Singapore;* orcid.org/0000-0003-1514-1271

Xingyu Chen − *School of Materials Science & Engineering, Nanyang Technological University, Singapore 639798, Singapore;* orcid.org/0009-0008-1719-5875

Ian P. Seetoh − *Temasek Laboratories, Nanyang Technological University, Singapore 637553, Singapore;* orcid.org/0000-0002-2951-9709

Guo Yao Lim − *School of Materials Science & Engineering, Nanyang Technological University, Singapore 639798, Singapore*

Wei Xin Tan − *School of Materials Science & Engineering, Nanyang Technological University, Singapore 639798, Singapore*

Vasanthan Thirunavukkarasu − *School of Physical and Mathematical Sciences, Nanyang Technological University, Singapore 637371, Singapore*

Tianli Jin − *School of Physical and Mathematical Sciences, Nanyang Technological University, Singapore 637371, Singapore;* orcid.org/0000-0002-9364-6024

Wen Siang Lew − *School of Physical and Mathematical Sciences, Nanyang Technological University, Singapore 637371, Singapore;* orcid.org/0000-0002-5161-741X

Complete contact information is available at: https://pubs.acs.org/10.1021/acsami.4c19118

Author Contributions

⊥A.K.R. and X.C. contributed equally to this work.

Notes

The authors declare no competing financial interest.

■ ACKNOWLEDGMENTS

The authors declare no conflicts of interest. The authors would like to thank Prof. Zhong Chen as his support was instrumental in the early stages of this research. We would like to acknowledge the Facility for Analysis, Characterisation, Testing and Simulation, Nanyang Technological University, Singapore, for use of their electron microscopy/X-ray facilities. This work was partially supported by C.Q.L's Nanyang Assistant Professorship grant (award no.: #022081-00001).

■ REFERENCES

(1) Dieny, B.; Prejbeanu, I. L.; Garello, K.; Gambardella, P.; Freitas, P.; Lehndorff, R.; Raberg, W.; Ebels, U.; Demokritov, S. O.; Akerman, J.; et al. Opportunities and challenges for spintronics in the microelectronics industry. *Nat. Electron.* **2020**, *3* (8), 446−459.

(2) Zuo, S.; Fan, H.; Nazarpour, K.; Heidari, H. A CMOS analog front-end for tunnelling magnetoresistive spintronic sensing systems. In *2019 IEEE International Symposium on Circuits and Systems (ISCAS)*; IEEE, 2019; pp 1−5.

(3) Chiu, Y.-C.; Khwa, W.-S.; Yang, C.-S.; Teng, S.-H.; Huang, H.-Y.; Chang, F.-C.; Wu, Y.; Chien, Y.-A.; Hsieh, F.-L.; Li, C.-Y.; et al. A CMOS-integrated spintronic compute-in-memory macro for secure AI edge devices. *Nat. Electron.* **2023**, *6* (7), 534−543.

(4) Lee, P.-H.; Lee, C.-F.; Shih, Y.-C.; Lin, H.-J.; Chang, Y.-A.; Lu, C.-H.; Chen, Y.-L.; Lo, C.-P.; Chen, C.-C.; Kuo, C.-H. 33.1 A 16nm 32Mb Embedded STT-MRAM with a 6ns Read-Access Time, a 1M-Cycle Write Endurance, 20-Year Retention at 150° C and MTJ-OTP Solutions for Magnetic Immunity. In *2023 IEEE International Solid-State Circuits Conference (ISSCC)*; IEEE, 2023; pp 494−496.

(5) Ramesh, A. K.; Chen, K.-M.; Lin, Y.-J.; Singh, P.; Wei, J.-H.; Hsin, Y.-C.; Wu, C.-I.; Tseng, Y.-C. Insertion trade-off effects on the

spin-transfer torque memory explored by In Situ x-ray. *ACS Appl. Electron. Mater.* **2021**, *3* (9), 4047−4055.
(6) Chavent, A.; Iurchuk, V.; Tillie, L.; Bel, Y.; Lamard, N.; Vila, L.; Ebels, U.; Sousa, R. C.; Dieny, B.; Di Pendina, G.; et al. A multifunctional standardized magnetic tunnel junction stack embedding sensor, memory and oscillator functionality. *J. Magn. Magn. Mater.* **2020**, *505*, 166647.
(7) Lee, T.; Lee, J.; Kim, M.; Oh, J.; Lee, J.; Jeong, H.; Jang, P.; Joo, M.; Suh, K.; Han, S. World-most energy-efficient MRAM technology for non-volatile RAM applications. In *2022 International Electron Devices Meeting (IEDM)*; IEEE, 2022; pp 10.7. 1−10.7. 4.
(8) Bhatti, S.; Sbiaa, R.; Hirohata, A.; Ohno, H.; Fukami, S.; Piramanayagam, S. Spintronics based random access memory: a review. *Mater. Today* **2017**, *20* (9), 530−548.
(9) Jung, Y.; Kim, M.; Jeong, S.; Hong, S.; Ko, S. H. Strain-Insensitive Outdoor Wearable Electronics by Thermally Robust Nanofibrous Radiative Cooler. *ACS Nano* **2024**, *18*, 2312−2324.
(10) Rana, V.; Gangwar, P.; Meena, J. S.; Ramesh, A. K.; Bhat, K.; Das, S.; Singh, P. A highly sensitive wearable flexible strain sensor based on polycrystalline MoS2 thin film. *Nanotechnology* **2020**, *31* (38), 385501.
(11) Cho, Y.; Kim, K.; Kim, D.; Bissannagari, M.; Lee, J.; Hong, W.; Kwon, H.-J.; Jang, J. E.; Kang, H. Stretchable Substrate Surface-Embedded Inkjet-Printed Strain Sensors for Design Customizable On-Skin Healthcare Electronics. *ACS Appl. Electron. Mater.* **2024**, *6*, 3147−3157.
(12) Luo, Y.; Abidian, M. R.; Ahn, J.-H.; Akinwande, D.; Andrews, A. M.; Antonietti, M.; Bao, Z.; Berggren, M.; Berkey, C. A.; Bettinger, C. J.; et al. Technology roadmap for flexible sensors. *ACS Nano* **2023**, *17* (6), 5211−5295.
(13) Zhang, Z.; Zhu, Z.; Zhou, P.; Zou, Y.; Yang, J.; Haick, H.; Wang, Y. Soft bioelectronics for therapeutics. *ACS Nano* **2023**, *17* (18), 17634−17667.
(14) Zhang, Y.; Li, P.; Quan, J.; Li, L.; Zhang, G.; Zhou, D. Progress, challenges, and prospects of soft robotics for space applications. *Adv. Intell. Syst.* **2023**, *5* (3), 2200071.
(15) Wang, S.; Xu, J.; Wang, W.; Wang, G.-J. N.; Rastak, R.; Molina-Lopez, F.; Chung, J. W.; Niu, S.; Feig, V. R.; Lopez, J.; et al. Skin electronics from scalable fabrication of an intrinsically stretchable transistor array. *Nature* **2018**, *555* (7694), 83−88.
(16) Wang, C.; Zhang, H.; Li, C.; He, Y.; Zhang, L.; Zhao, X.; Yang, Q.; Xian, D.; Mao, Q.; Peng, B.; et al. Voltage control of magnetic anisotropy through ionic gel gating for flexible spintronics. *ACS Appl. Mater. Interfaces* **2018**, *10* (35), 29750−29756.
(17) Hwee Wong, G. D.; Xu, Z.; Gan, W.; Ang, C. C. I.; Law, W. C.; Tang, J.; Zhang, W.; Wong, P. K. J.; Yu, X.; Xu, F.; et al. Strain-mediated spin−orbit torque enhancement in Pt/Co on flexible substrate. *ACS Nano* **2021**, *15* (5), 8319−8327.
(18) Zhao, S.; Zhou, Z.; Li, C.; Peng, B.; Hu, Z.; Liu, M. Low-voltage control of (Co/Pt) x perpendicular magnetic anisotropy heterostructure for flexible spintronics. *ACS Nano* **2018**, *12* (7), 7167−7173.
(19) Matsumoto, H.; Ota, S.; Ando, A.; Chiba, D. A flexible exchange-biased spin valve for sensing strain direction. *Appl. Phys. Lett.* **2019**, *114* (13), 132401.
(20) Ding, S.; Tian, Y.; Dong, H.; Zhu, D.; Hu, W. Anisotropic magnetoresistance in NiFe-based polymer spin valves. *ACS Appl. Mater. Interfaces* **2019**, *11* (12), 11654−11659.
(21) Bedoya-Pinto, A.; Donolato, M.; Gobbi, M.; Hueso, L. E.; Vavassori, P. Flexible spintronic devices on Kapton. *Appl. Phys. Lett.* **2014**, *104* (6), 062412.
(22) Chen, J.; Zhang, Z. A flexible anisotropic magnetoresistance sensor for magnetic field detection. *J. Mater. Sci.: Mater. Electron.* **2023**, *34* (1), 73.
(23) Is, F.; Mohanta, M. K.; Sarkar, A. D. Insights into selected 2D piezo Rashba semiconductors for self-powered flexible piezo spintronics: material to contact properties. *J. Phys.: Condens. Matter* **2023**, *35*, 253001.
(24) Sasmal, A.; Arockiarajan, A. Recent progress in flexible magnetoelectric composites and devices for next generation wearable electronics. *Nano Energy* **2023**, *115*, 108733.
(25) Bandyopadhyay, S.; Atulasimha, J.; Barman, A. Magnetic straintronics: Manipulating the magnetization of magnetostrictive nanomagnets with strain for energy-efficient applications. *Appl. Phys. Rev.* **2021**, *8* (4), 041323.
(26) Ramesh, A. K.; Rana, V.; Das, P.; Singh, P. Polycrystalline sense layer for magnetic tunnel junction (MTJ) as ultrasensitive sensing element for MEMS pressure sensors. In *2019 IEEE 32nd International Conference on Micro Electro Mechanical Systems (MEMS)*; IEEE, 2019; pp 99−102.
(27) Mondal, S.; Abeed, M. A.; Dutta, K.; De, A.; Sahoo, S.; Barman, A.; Bandyopadhyay, S. Hybrid magnetodynamical modes in a single magnetostrictive nanomagnet on a piezoelectric substrate arising from magnetoelastic modulation of precessional dynamics. *ACS Appl. Mater. Interfaces* **2018**, *10* (50), 43970−43977.
(28) Ramesh, A. K.; Chou, Y.-T.; Lu, M.-T.; Singh, P.; Tseng, Y.-C. Biological sensing using anomalous hall effect devices. *Nanotechnology* **2022**, *33* (33), 335502.
(29) Wang, K.; Zhang, Y.; Xiao, G. Anomalous Hall sensors with high sensitivity and stability based on interlayer exchange-coupled magnetic thin films. *Phys. Rev. Appl.* **2020**, *13* (6), 064009.
(30) Ning, J.; Zhao, Y.; Chen, Z.; Sun, Y.; Gao, Q.; Chen, Y.; Kanagaraj, M.; Zhang, J.; He, L. Ultra-sensitive anomalous Hall effect sensors based on Cr-doped Bi2Te3 topological insulator thin films. *J. Phys. D: Appl. Phys.* **2020**, *53* (50), 505001.
(31) Wong, G. D. H.; Ang, C. C. I.; Gan, W.; Law, W. C.; Xu, Z.; Xu, F.; Seet, C. S.; Lew, W. S. Reversible strain-induced spin−orbit torque on flexible substrate. *Appl. Phys. Lett.* **2021**, *119* (4), 042402.
(32) Chung, J.-C.; Anbalagan, A. k.; Fan, C.-L.; Liao, Y.-H.; Ramesh, A. K.; Gupta, S.; Tseng, Y.-C.; Tai, N.-H.; Lee, C.-H. Investigating the mechanism of magnetic phase transition temperature of FeRh thin films by doping copper impurities. *Mater. Chem. Phys.* **2022**, *275*, 125252.
(33) Zhang, Y.; Feng, X.; Zheng, Z.; Zhang, Z.; Lin, K.; Sun, X.; Wang, G.; Wang, J.; Wei, J.; Vallobra, P.; et al. Ferrimagnets for spintronic devices: From materials to applications. *Appl. Phys. Rev.* **2023**, *10* (1), 011301.
(34) Elphick, K.; Frost, W.; Samiepour, M.; Kubota, T.; Takanashi, K.; Sukegawa, H.; Mitani, S.; Hirohata, A. Heusler alloys for spintronic devices: review on recent development and future perspectives. *Sci. Technol. Adv. Mater.* **2021**, *22* (1), 235−271.
(35) Makushko, P.; Oliveros Mata, E. S.; Cañón Bermúdez, G. S.; Hassan, M.; Laureti, S.; Rinaldi, C.; Fagiani, F.; Barucca, G.; Schmidt, N.; Zabila, Y.; et al. Flexible magnetoreceptor with tunable intrinsic logic for on-skin touchless human-machine interfaces. *Adv. Funct. Mater.* **2021**, *31* (25), 2101089.
(36) Du, B.; Zhou, X.; Li, Q.; Liu, J.; Liu, Y.; Zeng, X.; Cheng, X.; Hu, H. Surface Treat Method to Improve the Adhesion between Stainless Steel and Resin: A Review. *ACS Omega* **2023**, *8* (43), 39984−40004.
(37) Kafkopoulos, G.; Karakurt, E.; Martinho, R. P.; Duvigneau, J.; Vancso, G. J. Engineering of Adhesion at Metal−Poly(lactic acid) Interfaces by Poly(dopamine): The Effect of the Annealing Temperature. *ACS Appl. Polym. Mater.* **2023**, *5* (7), 5370−5380.
(38) Zhang, F.-T.; Xu, L.; Chen, J.-H.; Zhao, B.; Fu, X.-Z.; Sun, R.; Chen, Q.; Wong, C.-P. Electroless deposition metals on poly (dimethylsiloxane) with strong adhesion as flexible and stretchable conductive materials. *ACS Appl. Mater. Interfaces* **2018**, *10* (2), 2075−2082.
(39) Chan, B. Q. Y.; Chong, Y. T.; Wang, S.; Lee, C. J. J.; Owh, C.; Wang, F.; Wang, F. Synergistic combination of 4D printing and electroless metallic plating for the fabrication of a highly conductive electrical device. *Chem. Eng. J.* **2022**, *430*, 132513.
(40) Georgieva, M.; Lazarova, D.; Petrova, M.; Tzaneva, B.; Dobreva, E. Modification of the surface of ABS polymer by swelling operation and its influence on some properties of electroless deposited metal coatings. *Trans. IMF* **2023**, *101* (1), 14−18.

(41) Nian, Y.-Y.; Chen, S.-C.; Chang, C.-P.; Luo, Z.-Y.; Ger, M.-D. Inkjet Catalyst Printing and Electroless Ni-P Deposition for Fabrication of WWAN Antenna on PC/ABS Substrate. *Int. J. Electrochem. Sci.* **2016**, *11* (11), 9762−9775.
(42) Tsai, J.-T.; Akin, S.; Zhou, F.; Park, M. S.; Bahr, D. F.; Jun, M. B.-G. Electrically conductive metallized polymers by cold spray and Co-electroless deposition. *ASME Open J. Eng.* **2022**, *1*, 011007.
(43) Vasconcelos, B.; Serra, R.; Oliveira, J.; Fonseca, C. Durable electroless deposited Ni-P films on NBR for dynamic contacts. Characterization and tribological performance. *Surf. Coat. Technol.* **2021**, *423*, 127579.
(44) Park, S. J.; Ko, T.-J.; Yoon, J.; Moon, M.-W.; Oh, K. H.; Han, J. H. Copper circuit patterning on polymer using selective surface modification and electroless plating. *Appl. Surf. Sci.* **2017**, *396*, 1678−1684.
(45) Sharma, M.; Kuanr, B. K. Magnetization Dynamics of Ferromagnetic Nanostructures for Spintronics and Biomedical Applications. In *Nanoparticles in Diagnosis, Drug Delivery and Nanotherapeutics*; CRC Press, 2024; pp 44−81.
(46) Hait, S.; Barwal, V.; Gupta, N. K.; Pandey, L.; Mishra, V.; Chaudhary, S. Influence of annealing temperature and capping layer on the structural, magnetic and transport properties of ion beam sputtered Co2FeAl thin films on Si (1 0 0). *Appl. Surf. Sci.* **2022**, *572*, 151423.
(47) Lee, H.; Dellatore, S. M.; Miller, W. M.; Messersmith, P. B. Mussel-inspired surface chemistry for multifunctional coatings. *Science* **2007**, *318* (5849), 426−430.
(48) Ding, Y.; Floren, M.; Tan, W. Mussel-inspired polydopamine for bio-surface functionalization. *Biosurface and Biotribology* **2016**, *2* (4), 121−136.
(49) Manoj, T.; Kotha, S.; Paikaray, B.; Srideep, D.; Haldar, A.; Rao, K. V.; Murapaka, C. Giant spin pumping at the ferromagnet (permalloy)−organic semiconductor (perylene diimide) interface. *RSC Adv.* **2021**, *11* (56), 35567−35574.
(50) Seetoh, I. P.; Ramesh, A. K.; Tan, W. X.; Lai, C. Enhanced photoelectrochemical water splitting using carbon cloth functionalized with ZnO nanostructures via polydopamine assisted electroless deposition. *Nanoscale* **2024**, *16*, 8401−8416.
(51) Ryu, J. H.; Messersmith, P. B.; Lee, H. Polydopamine Surface Chemistry: A Decade of Discovery. *ACS Appl. Mater. Interfaces* **2018**, *10* (9), 7523−7540.
(52) Ding, Y.; Weng, L.-T.; Yang, M.; Yang, Z.; Lu, X.; Huang, N.; Leng, Y. Insights into the aggregation/deposition and structure of a polydopamine film. *Langmuir* **2014**, *30* (41), 12258−12269.
(53) Yang, Z.; Tu, Q.; Zhu, Y.; Luo, R.; Li, X.; Xie, Y.; Maitz, M. F.; Wang, J.; Huang, N. Mussel-inspired coating of polydopamine directs endothelial and smooth muscle cell fate for re-endothelialization of vascular devices. *Adv. Healthcare Mater.* **2012**, *1* (5), 548−559.
(54) Wagner, C. D. *NIST X-ray Photoelectron Spectroscopy Database*; NIST Standarad Reference Database 20, 2000.
(55) Sun, Q.-Y.; Li, Z.; Xu, Z.; Zheng, Z.-J.; Cao, J.; Yang, K.-F.; Cui, Y.-M.; Xu, L.-W. PdCl2(CH3CN)2-catalyzed regioselective C−H olefinations of 2-amino biaryls with vinylsilanes as unactivated alkenes. *Chem. Commun.* **2019**, *55* (44), 6229−6232.
(56) Pérez-Alonso, F.; Adán, C.; Rojas, S.; Peña, M.; Fierro, J. Ni−Co electrodes prepared by electroless-plating deposition. A study of their electrocatalytic activity for the hydrogen and oxygen evolution reactions. *Int. J. Hydrogen Energy* **2015**, *40* (1), 51−61.
(57) Goyat, E.; Pandey, L.; Hait, S.; Gupta, N. K.; Mishra, V.; Kumar, N.; Singh, H.; Sharma, N.; Chaudhary, S. Effect of the growth rate on the structural, magnetic and transport properties of NiFe thin films. *J. Mater. Sci.: Mater. Electron.* **2023**, *34* (13), 1111.
(58) Kharmouche, A.; Cherrad, O. Structural, microstructural and morphological properties of Permalloy/Si (100) thin films. *Phys. B* **2024**, *680*, 415803.
(59) Hait, S.; Husain, S.; Bangar, H.; Pandey, L.; Barwal, V.; Kumar, N.; Gupta, N. K.; Mishra, V.; Sharma, N.; Gupta, P.; et al. Spin Pumping through Different Spin−Orbit Coupling Interfaces in β-W/Interlayer/Co_2FeAl Heterostructures. *ACS Appl. Mater. Interfaces* **2022**, *14* (32), 37182−37191.
(60) Meier, T. *Ferromagnetische Resonanz (FMR)*; Technische Universität München, 2020.
(61) Kalarickal, S. S.; Krivosik, P.; Das, J.; Kim, K. S.; Patton, C. E. Microwave damping in polycrystalline Fe-Ti-N films: Physical mechanisms and correlations with composition and structure. *Phys. Rev. B:Condens. Matter Mater. Phys.* **2008**, *77* (5), 054427.
(62) Husain, S.; Akansel, S.; Kumar, A.; Svedlindh, P.; Chaudhary, S. Growth of Co2FeAl Heusler alloy thin films on Si (100) having very small Gilbert damping by Ion beam sputtering. *Sci. Rep.* **2016**, *6* (1), 28692.
(63) Kwon, J.-H.; Kwak, W.-Y.; Cho, B. K. Magnetization manipulation of a flexible magnetic sensor by controlled stress application. *Sci. Rep.* **2018**, *8* (1), 15765.
(64) Wang, P.-C.; Liu, Y.-M.; Chang, C.-P.; Liao, Y.-Y.; Peng, Y.-Y.; Ger, M.-D. A laser curable palladium complex ink used for fabrication of copper pattern on polyimide substrate. *J. Taiwan Inst. Chem. Eng.* **2017**, *80*, 963−969.
(65) Akin, S.; Nath, C.; Jun, M. B.-G. Selective Surface Metallization of 3D-Printed Polymers by Cold-Spray-Assisted Electroless Deposition. *ACS Appl. Electron. Mater.* **2023**, *5* (9), 5164−5175.
(66) Rauta, C. S.; Majumdar, G.; Mukherjee, S.; Sarkar, S. An eco-friendly one-step pretreatment method for the synthesis of electroless coating on magnesium alloy. *Phys. Scr.* **2024**, *99* (10), 105934.
(67) Jiang, D.; Wang, D.; Liu, G.; Wei, Q. Atomic oxygen adaptability of flexible Kapton/Al2O3 composite thin films prepared by ion exchange method. *Coatings* **2019**, *9* (10), 624.
(68) Lee, H. A.; Park, E.; Lee, H. Polydopamine and its derivative surface chemistry in material science: a focused review for studies at KAIST. *Adv. Mater.* **2020**, *32* (35), 1907505.
(69) Lee, H.; Scherer, N. F.; Messersmith, P. B. Single-molecule mechanics of mussel adhesion. *Proc. Natl. Acad. Sci. U.S.A.* **2006**, *103* (35), 12999−13003.
(70) Tian, J.; Qi, X.; Li, C.; Xian, G. Mussel-inspired fabrication of an environment-friendly and self-adhesive superhydrophobic polydopamine coating with excellent mechanical durability, anti-icing and self-cleaning performances. *ACS Appl. Mater. Interfaces* **2023**, *15* (21), 26000−26015.

https://doi.org/10.1021/acsami.4c19118
ACS Appl. Mater. Interfaces 2025, 17, 12805−12817